Investigating the influence of a weak continuous-wave-trigger on picosecond supercontinuum generation

Qian Li,[1] Feng Li,[1] Kenneth K. Y. Wong,[2] Alan Pak Tao Lau,[3] Kevin K. Tsia,[2] and P. K. A. Wai[1,*]

[1]*Photonics Research Centre, Department of Electronic and Information Engineering, The Hong Kong Polytechnic University, Hong Kong*
[2]*Department of Electrical and Electronic Engineering, The University of Hong Kong, Hong Kong*
[3]*Photonics Research Centre, Department of Electrical Engineering, The Hong Kong Polytechnic University, Hong Kong*
*enwai@polyu.edu.hk

Abstract: We numerically study the impacts of introducing a minute continuous-wave (CW) trigger on the properties of picosecond supercontinuum (SC) generation. We show that this simple triggering approach enables active control of not only the bandwidth, but more importantly the temporal coherence of SC. Detailed numerical simulations suggest that depending on the wavelength of the CW-trigger the multiple higher-order four-wave mixing (FWM) components generated by the CW-trigger can create either a relatively more stochastic or a more deterministic beating effect on the pump pulse, which has significant implications on how soliton fission and the onset of SC are initiated in the presence of noise. By controlling the CW-trigger wavelengths, the rogue solitons emerged in SC generation can exhibit high-degree of temporal coherence and pulse-to-pulse intensity stability. The present study provides a valuable insight on how the initial soliton fission can be initiated in a more controllable manner such that SC generation with both high temporal coherence and stability can be realized.

©2011 Optical Society of America

OCIS codes: (060.4370) Nonlinear optics, fibers; (320.6629) Supercontinuum generation

References and links

1. B. R. Washburn and N. R. Newbury, "Phase, timing, and amplitude noise on supercontinua generated in microstructure fiber," Opt. Express **12**(10), 2166–2175 (2004).
2. J. M. Dudley, G. Genty, and S. Coen, "Supercontinuum generation in photonic crystal fiber," Rev. Mod. Phys. **78**(4), 1135–1184 (2006).
3. Y. Han and B. Jalali, "Photonic time-stretched analog-to-digital converter: fundamental concepts and practical considerations," J. Lightwave Technol. **21**(12), 3085–3103 (2003).
4. D. L. Marks, A. L. Oldenburg, J. J. Reynolds, and S. A. Boppart, "Study of an ultrahigh-numerical-aperture fiber continuum generation source for optical coherence tomography," Opt. Lett. **27**(22), 2010–2012 (2002).
5. K. Goda, K. K. Tsia, and B. Jalali, "Serial time-encoded amplified imaging for real-time observation of fast dynamic phenomena," Nature **458**(7242), 1145–1149 (2009).
6. K. Goda, D. Solli, K. K. Tsia, and B. Jalali, "Theory of amplified dispersive Fourier transformation," Phys. Rev. A **80**(4), 043821 (2009).
7. G. E. Busch, R. P. Jones, and P. M. Rentzepis, "Picosecond spectroscopy using a picosecond continuum," Chem. Phys. Lett. **18**(2), 178–185 (1973).
8. C. Lin and R. H. Stolen, "New nanosecond continuum for excited-state spectroscopy," Appl. Phys. Lett. **28**(4), 216 (1976).
9. M. Maus, E. Rousseau, M. Cotlet, G. Schweitzer, J. Hofkens, M. Van der Auweraer, F. C. De Schryver, and A. Krueger, "New picosecond laser system for easy tunability over the whole ultraviolet/visible/near infrared wavelength range based on flexible harmonic generation and optical parametric oscillation," Rev. Sci. Instrum. **72**(1), 36 (2001).
10. A. B. Rulkov, M. Y. Vyatkin, S. V. Popov, J. R. Taylor, and V. P. Gapontsev, "High brightness picosecond all-fiber generation in 525-1800nm range with picosecond Yb pumping," Opt. Express **13**(2), 377–381 (2005).

11. M. Okuno, H. Kano, P. Leproux, V. Couderc, and H. O. Hamaguchi, "Ultrabroadband (>2000 cm^{-1}) multiplex coherent anti-Stokes Raman scattering spectroscopy using a subnanosecond supercontinuum light source," Opt. Lett. **32**(20), 3050–3052 (2007).
12. K. Tai, A. Tomita, J. L. Jewell, and A. Hasegawa, "Generation of subpicosecond solitonlike optical pulses at 0.3 THz repetition rate by induced modulational instability," Appl. Phys. Lett. **49**(5), 236 (1986).
13. A. S. Gouveia-Neto, M. E. Faldon, and J. R. Taylor, "Raman amplification of modulational instability and solitary-wave formation," Opt. Lett. **13**(11), 1029–1031 (1988).
14. D. R. Solli, C. Ropers, and B. Jalali, "Active control of rogue waves for stimulated supercontinuum generation," Phys. Rev. Lett. **101**(23), 233902 (2008).
15. D. R. Solli, C. Ropers, P. Koonath, and B. Jalali, "Optical rogue waves," Nature **450**(7172), 1054–1057 (2007).
16. D. R. Solli, B. Jalali, and C. Ropers, "Seeded supercontinuum generation with optical parametric down-conversion," Phys. Rev. Lett. **105**(23), 233902 (2010).
17. G. Genty, J. M. Dudley, and B. Eggleton, "Modulation control and spectral shaping of optical fiber supercontinuum generation in the picosecond regime," Appl. Phys. B **94**(2), 187–194 (2009).
18. A. Kudlinski, B. Barviau, A. Leray, C. Spriet, L. Héliot, and A. Mussot, "Control of pulse-to-pulse fluctuations in visible supercontinuum," Opt. Express **18**(26), 27445–27454 (2010).
19. K. K. Y. Cheung, C. Zhang, Y. Zhou, K. K. Y. Wong, and K. K. Tsia, "Manipulating supercontinuum generation by minute continuous wave," Opt. Lett. **36**(2), 160–162 (2011).
20. R. H. Stolen, J. P. Gordon, W. J. Tomlinson, and H. A. Haus, "Raman response function of silica-core fibers," J. Opt. Soc. Am. B **6**(6), 1159 (1989).
21. J. M. Dudley, G. Genty, and B. J. Eggleton, "Harnessing and control of optical rogue waves in supercontinuum generation," Opt. Express **16**(6), 3644–3651 (2008).
22. G. Genty, C. M. de Sterke, O. Bang, F. Dias, N. Akhmediev, and J. M. Dudley, "Collisions and turbulence in optical rogue wave formation," Phys. Lett. A **374**(7), 989–996 (2010).
23. D. V. Skryabin and A. V. Gorbach, "Colloquim: Looking at a soliton through the prism of optical supercontinuum," Rev. Mod. Phys. **82**(2), 1287–1299 (2010).
24. J. M. Dudley, G. Genty, F. Dias, B. Kibler, and N. Akhmediev, "Modulation instability, Akhmediev Breathers and continuous wave supercontinuum generation," Opt. Express **17**(24), 21497–21508 (2009).

1. Introduction

Supercontinuum (SC) generation in optical fibers is widely recognized as one of the salient research areas in nonlinear optics for decades. A captivating feature of SC is its ultrawideband spectrum which has been successfully utilized in a wide range of applications, such as optical frequency metrology [1], generation of ultrashort optical pulses [2], photonic time stretch analog-to-digital conversion [3], and optical coherence tomography [4]. Nevertheless, achieving a robust control of the stability of SC remains a critical challenge in many areas especially for those which require real-time, ultrafast and single-shot spectral measurements [5,6]. Although it is well known that SC stability can be greatly improved using femtosecond pulses, such ultrashort pulses require dedicated dispersion control and are often sensitive to perturbations. SC sources with longer pump pulses (e.g. picosecond or nanosecond) are hence more practical and indeed have mostly been utilized in a myriad of biophotonics applications [7–11].

An important nonlinear process in SC generated with long pulses is modulation instability (MI) growth, which is initiated spontaneously from noise. Hence, the resultant SC is inherently incoherent and unstable [12–14]. Solli et al. have shown that the amplified noise by MI can, in its extreme form, leads to a small number of statistically-rare "rogue" events in picosecond SC [15]. Afterwards, there have been great interests in the study of optical rogue waves in SC, which is a noise-sensitive nonlinear process exhibiting extreme value statistics. More interestingly, prior works have shown that control of the rogue waves in SC can be realized by using a pulse seed [14,16] or a direct THz intensity modulation of the input pulse [17]. Control of pulse-to-pulse fluctuations in visible SC was also demonstrated by using a dispersion-engineered photonic crystal fiber [18]. In contrast, we have experimentally demonstrated a simple triggering mechanism to manipulate SC generation by introducing a minute continuous wave (CW) light [19]. Our CW-triggering technique requires only wavelength tuning and thus represents a handy approach to achieve active control of SC. Injecting a weak CW within the MI gain spectral regions can significantly alter the output SC spectrum (thus the power) and the stability of the pulses when compared with the untriggered case (see Fig. 1) [19]. When the CW-trigger experiences cumulative MI gain in the early stage of SC generation, it accelerates the soliton fission process which leads to drastic spectral

broadening through Raman-induced self-frequency shift (RIFS) [12,19]. Hence, SC spectrum shows a significant red-shifted spectral component, typically called Raman soliton, which in turn generates the blue-shifted dispersive wave components in SC. This results in a dramatic enhancement in SC bandwidth and power.

In this paper, we numerically study how a minute continuous-wave (CW) trigger can affect the properties of the picosecond supercontinuum (SC) generation in detail. Simulations reveal that such a weak CW-trigger (100 – 10,000 times weaker than the pump) can actively control not only the bandwidth of SC but also its temporal coherence – supporting our previous experimental findings [19]. By simply varying the CW-trigger's wavelength, we are able to study in detail how the key SC characteristics (namely the bandwidth, the temporal coherence and the pulse-to-pulse stability) can be manipulated. In particular, we observe that the enhancement in SC bandwidth in general can be achieved at the expense of temporal coherence, or vice versa. More interestingly, we find that, depending on the CW-trigger wavelength, the multiple higher-order four-wave mixing (FWM) components generated by a CW-trigger can create either more deterministic or more stochastic beating effect on the pump pulse in the initial stage of SC generation. This might have a significant implication of how the subsequent Akhmediev breather (AB) condition and hence the soliton fission can be established in the presence of noise – leading to significant spectral broadening in SC. We show that by selecting the appropriate CW-trigger wavelengths, the "rogue" soliton emerged in SC generation can be controlled to exhibit high-degree temporal coherence and reduced pulse-to-pulse intensity fluctuation. The present work provides an important insight on how to further control and optimize the coherence and stability of longer-pulse (i.e. picoseconds or nanoseconds) SC, which is typically initiated by noisy MI growth, CW triggering scheme, or other approaches.
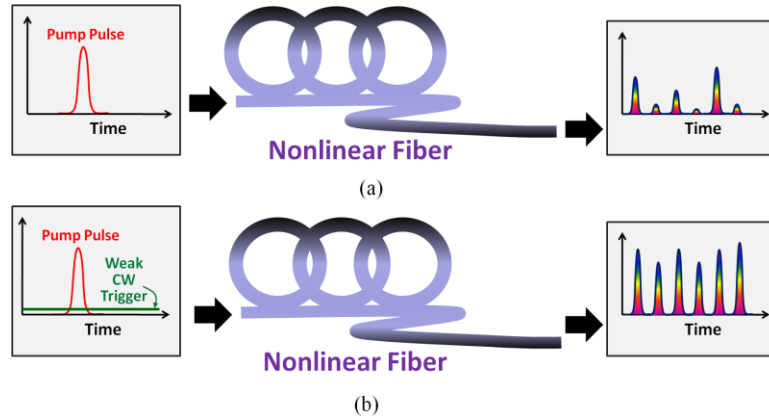

Fig. 1. Schematics of the (a) untriggered and (b) CW-triggered SC generation. If the CW-trigger wavelength can be tuned such that it can experience MI gain, the resultant SC characteristics, such as the bandwidth, power, and the pulse-to-pulse fluctuation, can be modified.

2. Numerical model

Our numerical model is based on the generalized nonlinear Schrödinger equation (GNLSE) [2]:

$$\frac{\partial A}{\partial z} + i\frac{\beta_2}{2}\frac{\partial^2 A}{\partial t^2} - \frac{\beta_3}{6}\frac{\partial^3 A}{\partial t^3} = i\gamma\left(1 + i\tau_{shock}\frac{\partial}{\partial t}\right)A(z,t)\int_{-\infty}^{+\infty} R(t')\left|A(z,t-t')\right|^2 dt', \quad (1)$$

where $A(z,t)$ is the field envelope, $\tau_{shock} = 1/\omega_0$ where ω_0 is the center frequency, β_2, β_3 and γ are the second-, third-order dispersion and nonlinear coefficient of the fiber respectively. The

Raman response function is given by $R(t)=(1-f_{\scriptscriptstyle R})\delta(t)+f_{\scriptscriptstyle R}h_{\scriptscriptstyle R}(t)$. We use $f_R = 0.18$ and $h_{\scriptscriptstyle R}$ determined from the experimental fused silica Raman cross-section [20]. We include the input random phase noise in the frequency domain through one photon per mode spectral density on each spectral grid in the simulation [21]. The specific value of the noise amplitude is not critical as it only influences the rogue wave generation rate [15]. The noise amplitude is chosen to be 10^{-6} of the pump amplitude. The model includes the higher-order dispersion up to the third order and all the nonlinear terms including the full Raman response (Eq. (1)). We note that the third order dispersion (TOD) plays a critical role in rogue soliton emergence by the early soliton collision process. It has recently been reported that an NLSE with only TOD perturbation can also result in rogue soliton features and are qualitatively similar to those observed with the full GNLSE [22]. We simulate a 5.8-ps FWHM chirp-free Gaussian pulse ($\sqrt{P_{\scriptscriptstyle 0}}\exp(-t^2/2/T_{\scriptscriptstyle 0}^2)$) with pulse width $T_0 = 3.5$ ps , peak power $P_{\scriptscriptstyle 0}$ = 60 W and center wavelength at 1554.5 nm propagating in a commercially available 50-m highly nonlinear dispersion-shifted fiber (HNL-DSF) with the zero dispersion wavelength (ZDW) at 1554 nm, the nonlinear coefficient γ = 14/W/km, and the second-order and third-order dispersion coefficients at the 1554.5 nm pump wavelength are β_2 = –0.0224 ps²/km and β_3 = 0.0576 ps³/km respectively. A weak CW-trigger $\sqrt{\varepsilon P_0}\exp(i\Omega t/T_0)$ is added together with the pump pulse at the input. The parameter ε is the relative CW-trigger intensity (compared to the pump power P_0) and Ω is the normalized frequency of the CW-trigger. The wavelength of the CW-trigger can be easily calculated by $\lambda = \lambda_0 - 2\pi c T_0/\Omega$, where λ_0 , T_0 and c are the center wavelength, pulse width and speed of light in vacuum, respectively.

3. Numerical results and discussion

We first study the impacts of the CW-trigger on SC bandwidth, coherence and pulse-to-pulse intensity statistics. We fix the wavelength of the CW-trigger at 1624 nm (Ω = –179.7) which is well within the MI gain spectrum of the fiber, similar to our previous experiment [19]. The CW-trigger power is set to be only 1% of the pump power. Figures 2(a) and 2(d) show respectively the untriggered and CW-triggered SC spectra. Clearly, SC bandwidth is significantly widened under the CW-triggering condition. The CW-trigger extends the bandwidth at the −50 dB level from 787 nm (1260 to 2047 nm) to 933 nm (1220 to 2153 nm). As described, such bandwidth enhancement can be understood by that the cumulative MI gain acquired by the CW-trigger facilitates the initiation of soliton fission − a key process contributing to significant spectral broadening.

   We also calculate the first-order temporal coherence $|g_{12}(\lambda)|$ of SC using the method described in [4]. Note that $|g_{12}(\lambda)|$ lies in the interval [0,1], and a value of 1 denotes perfect coherence. Compared with the case of untriggered SC in which only a narrow band close to the pump center wavelength has relatively good coherence (Fig. 2(b)), the CW-triggered SC shows a better coherence especially in the two additional spectral sidebands (Fig. 2(e)). The high coherence in these two bands can be attributed to the coherent energy transfer via four-wave mixing (FWM) among the spectrally-broadened pump (~1554nm), the CW-trigger (1624 nm) and the generated idler (~1490 nm).

   As we will discuss later, the CW-trigger considerably affects the initial soliton fission which generates a red-shifted "rogue" soliton, we thus particularly study the pulse-to-pulse fluctuation in this red-shifted spectral range. For each SC in the simulation ensemble, we apply a long-pass spectral filter to select the red-shifted part of SC. Fourier transformation yields a series of ultrashort temporal pulses, which are then used to plot their intensity statistics. Figure 2(c) shows the peak power histogram for 1000 events after a long-pass filter (>1850 nm). Note that only the pulses with peak powers larger than the pump power, and pulse-to-pulse separation within one simulation run larger than the average pulse width are counted. It can be observed that the peak power histogram of the untriggered SC has a long tail distribution which is a signature of the extreme-value statistics (Fig. 2(c)). In contrast, the

CW-trigger changes the statistics into an almost Gaussian distribution (see the yellow Gaussian fitting curve) (Fig. 2(f)). This illustrates that the CW-triggering process causes the rare events to become the norm. As a result, adding a minute CW-trigger in SC generation, the resulting SC can be greatly modified in terms of bandwidth, temporal coherence, and pulse-to-pulse statistics. This is in an excellent agreement with our previous experiment [19].

We then study in detail how SC characteristics can be affected by varying the CW-trigger wavelength. In general, SC bandwidth first increases for small Ω until $\Omega = -200$ where the bandwidth is at its maximum. The bandwidth then decreases with Ω (as shown in Fig. 3(a)). This trend is consistent with our previous experimental results [19] that the bandwidth of SC reaches to its maximum when the trigger wavelength is close to the MI peak shift ($\Omega = -200$ in this case). Hence, Fig. 3(a) further confirms that the bandwidth enhancement in SC generally correlates with the MI gain experienced by the CW-trigger, depending on its wavelength. Stronger MI growth means that the soliton fission is relatively easier to be initiated by the CW-trigger (rather than noise). It thus facilitates the subsequent RIFS which enhances the red-shift of the Raman soliton and the blue-shift of the dispersive waves in SC. The short-wavelength generation of the SC can be attributed to the pulse-trapping effect originated from the interplay between the accelerating solitons and the wave packet which is in the normal-dispersion regime [23]. As the CW-trigger moves to the longer wavelengths, its MI growth becomes weakened and the final SC bandwidth will then be reduced.
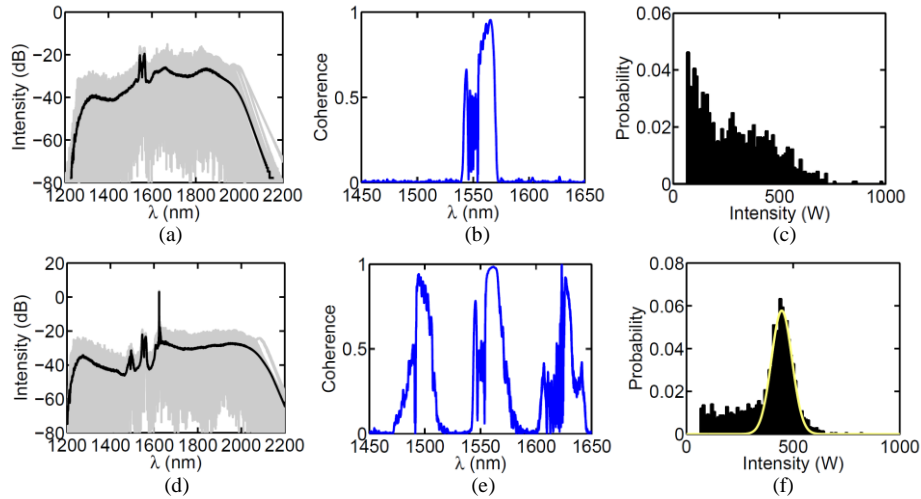

Fig. 2. Comparisons between (a, b, c) the untriggered SC and (d, e, f) the CW-triggered SC. (a) The untriggered and (d) the CW-triggered SC spectra. The individual spectra from the simulation ensemble (gray; for clarity only 50 shots are plotted) with the calculated average spectrum from the 1000 simulation runs (back curve); The first-order temporal coherence of the (b) untriggered and (e) CW-triggered SC; The histograms of the peak power distribution of the (c) untriggered and (f) CW-triggered SC. The histograms are plotted for the 1000 events after a long-pass filter (>1850 nm) using 10 W bins.

Interestingly, we find that the temporal coherence exhibits the opposite trend as a function of the CW-trigger wavelengths (Fig. 3(b)). The coherence bandwidth shrinks to a minimum at $\Omega = -200$. It then increases as the CW-trigger wavelength moves further away from the pump. At $\Omega = -50$, the temporal coherence remains relatively high, albeit showing complicated undulation features, from 1400 to 1800 nm. The coherence bandwidth reaches to its minimum at $\Omega = -200$ where the high coherence can be found in three main spectral bands. As Ω increases, the separation between the three bands and their bandwidths increase accordingly. Note that the frequencies of the three bands are well consistent with the FWM relation. It suggests that the high coherence in these bands originates from the coherent parametric FWM process. A striking feature (will be discussed later) can be observed at $\Omega = -400$ where the

coherence in the red-shifted Raman soliton (1850 – 2000 nm, in the bottom plot of Fig. 3(b)) shows a drastic improvement.

Figures 4(a) and 4(b) further highlight the dependence of SC bandwidth and coherence properties on the CW-trigger wavelengths where both negative (solid dots) and positive Ω (circles) are included. Figure 4(a) shows the average SC bandwidth (calculated from 200 simulations for each Ω) at –50 dB level. Again, we observe the increase in bandwidth for small $|\Omega|$ followed by the decreasing trend as $|\Omega|$ is larger. The maximum bandwidth is attained at $|\Omega|$ ~200. Both positive and negative Ω show the similar trends. It is useful to introduce a spectrally averaged coherence $\langle |g_{12}| \rangle = \int |g_{12}(\lambda,0)| |E(\lambda)|^2 \, d\lambda / \int |E(\lambda)|^2 \, d\lambda$ in order to quantify the overall coherence across SC spectrum [2], as illustrated in Fig. 4(b). For each Ω, $\langle |g_{12}| \rangle$ is calculated from an ensemble of 200 simulations in the 1200 – 2200 nm wavelength range. We note that the difference between $\langle |g_{12}| \rangle$ obtained from 200 and 1000 simulations is less than 1%. Generally speaking, introducing the CW-trigger can improve the overall temporal coherence of SC when compared with the untriggered SC (see the dashed line). $\langle |g_{12}| \rangle$ is only 0.155 for the untriggered SC (dashed line), while $\langle |g_{12}^{(1)}| \rangle$ varies roughly from 0.4 to 0.6 for the CW-triggered SC. Again, we can see that the coherence of SC follows the opposite trend when compared with SC bandwidth (Fig. 4(a)). In particular, when we plot the average coherence for the wavelengths longer than 1850 nm, this red-shifted part of SC is generally incoherent ($\langle |g_{12}^{(1)}| \rangle$ ~0.005) except when $\Omega = -400$ where the average coherence is as high as 0.745 (not shown in Fig. 4(c)). It suggests that the red-shifted part of SC (mainly the Raman soliton) does not show obvious temporal coherence improvement when the CW-trigger is introduced except when the trigger is tuned to a certain longer wavelength ($\Omega = -400$ in this case). This intriguing feature will be discussed shortly. This spectrally long-passed average coherence (>1850 nm) can be used later to explain the pulse-to-pulse intensity variations of the Raman soliton.
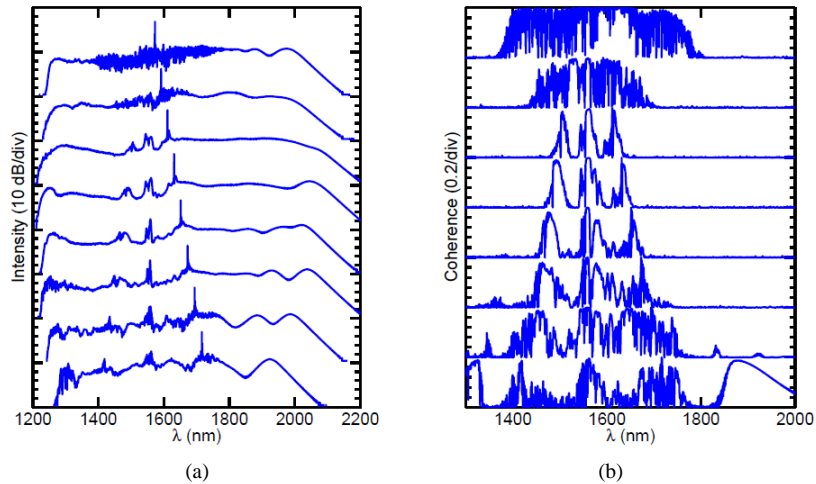

(a)   (b)

Fig. 3. (a) The CW-triggered SC spectra and (b) the corresponding temporal coherence spectra for $\Omega = -50, -100, -150, -200, -250, -300, -350,$ and -400 ($\lambda = 1573, 1592, 1612, 1631, 1652, 1673, 1694,$ and 1716 nm, from top to bottom) respectively.
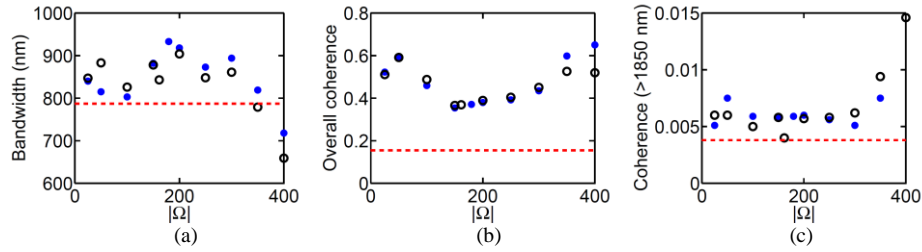
Fig. 4. (a) The bandwidths of the CW-triggered SC spectra (measured at −50 dB level in Fig. 3(a)) versus $|\Omega|$; (b) The overall temporal coherence of the CW-triggered SC spectra versus $|\Omega|$; (c) the temporal coherence beyond the 1850 nm CW-triggered SC spectra versus $|\Omega|$. Note that for $\Omega = -400$, the coherence (>1850 nm) is as high as 0.745 (not shown in the plot). Dots and circles represent the results for negative and positive Ω, respectively. The dashed lines represent the results of the untriggered SC.

Figures 5, 6 and 7 show the spectral and temporal evolutions in SC generation along the fiber (with a length of 50 m) without the CW-trigger, with the CW-trigger at $\Omega = -179.7$ and −400, respectively, each from a representative single-shot SC simulation showing the prominent Raman soliton feature. The spectral and the temporal shapes are shown in every 5 m (from bottom to top). In these results, the input random noise is included as described in Section 2 so that the initial evolution dynamic for each case can be practically modeled. It should be emphasized that the differences in the evolution dynamics among these three representative cases explain well the general statistical effects of noise which are studied in detail in Figs. 2 and 8 Figure 5(a) shows that the MI sidebands spontaneously grow from noise in the initial stage (0 − 20 m) until the MI sidebands develop into the triangular spectral wings at 25 m. This point is believed to be the onset of the higher order effects, e.g. soliton fission, TOD, and RIFS, which result in the sizable spectral broadening in SC (25 − 50 m) [24]. It has recently been reported that the initial MI evolution (before the onset of SC) can be interpreted as the Akhmediev Breather (AB) dynamics which develops a complex modulated temporal profile on the pump pulse [24]. The ABs serve as the precursors for soliton fission by forming the "pre-solitonic" pulses, which can be observed at 25 m (see the inset of Fig. 5(b)). The AB frequency components which experience the high MI gain are expected to be the predominant factors to build up the "pre-solitonic" pulses and thus result in the soliton fission. The Raman rogue soliton can then be developed through RIFS as well as TOD − increasing the red-shift and the time delay with respect to the original pump pulse (from 25 to 50 m in Figs. 5(a) and 5(b)).
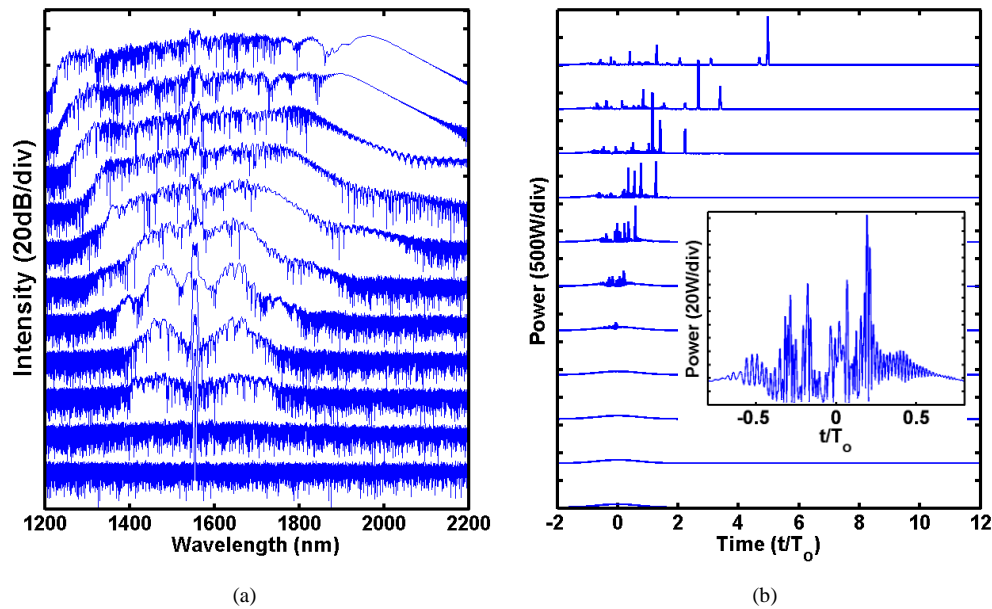
Fig. 5. (a) Spectral and (b) temporal evolution for untriggered SC generation. The spectra and temporal pulse shapes are shown in every 5 m (from bottom to top, $z = 0$, 5, 10, …, 50 m). The inset shows the enlarged view of the temporal pulse at 25 m.

Figure 6 depicts SC evolution with the CW-trigger at $\Omega = -179.7$. This CW-trigger wavelength is chosen to match the MI gain peak identified at 20 m in the case of untriggered SC (see Fig. 5(a)). Note that it is also the wavelength which gives rise to the maximum bandwidth, as shown in Fig. 4(a). In the early stage of the evolution, progressive parametric wavelength conversion via FWM can be observed (from 0 to 20 m). Figure 6 shows that these higher-order FWM components together with the original CW-trigger compete with each other for the same MI gain in the presence of noise. Hence, the superposition of these competing FWM components introduces a complex beating effect on the pump pulse – bringing the pulse into the AB evolution. It should be emphasized that the AB is now developed in the temporal pulse not only by broadband noise but also predominantly due to the multiple "FWM triggers". It can be verified by the beating frequencies imposed on the temporal pulse at 20 m, as shown in the inset of Fig. 6(b). As a result, the AB evolution is accelerated by such CW-triggering and hence, the subsequent rogue soliton frequency down-shifting as well as its time delay are greatly enhanced – leading to considerable spectral broadening.

When the CW-trigger is tuned to the longer wavelength at $\Omega = -400$, similar multiple FWM processes can be seen in the initial stage of the evolution with this trigger (see Fig. 7(a)). Remarkably, the onset of SC appears to be much earlier than that of the untriggered SC and SC with the trigger at $\Omega = -179.7$ (compared with Figs. 5(a) and 6(a)). Furthermore, the rate of the subsequent RIFS of the Raman soliton is slower than that of $\Omega = -179.7$ (compared with Fig. 6(b)). This is consistent with Fig. 4(a) that the longer-wavelength CW-trigger results in less spectral broadening. We have seen that the Raman soliton exhibits impressively high temporal coherence (shown in Fig. 3(b)) when the CW-trigger is tuned to $\Omega = -400$. The observed phenomenon could be explained as follow. Although the CW-trigger wavelength is not chosen to be at the MI gain peak, initially the CW-trigger can still experience moderate MI gain as observed in the coherent parametric FWM shown in Fig. 7(a). However, since the pump is continuously weakened by the parametric conversion process, the MI gain peak decreases and its gain bandwidth narrows dynamically along the fiber. After a certain distance, the CW-trigger (at $\Omega = -400$) will be outside the MI gain spectrum. The MI gain

spectral shift and narrowing apply to both untriggered and CW-triggered SC. This effect is evident in the case of untriggered SC (Fig. 5(a)). In addition, the higher-order FWM in this case is significantly less efficient because the higher-order components are far outside the MI gain spectrum. Thus only the first-order FWM components are dominant within the MI gain spectrum. As a result, (1) no higher-order FWM components compete for the same MI gain, and (2) the AB evolution is less vulnerable to noise growth because it does not experience the highest MI gain. Therefore, the resultant AB evolution is subject to a more deterministic initial condition, i.e. determined by the growing CW-trigger with reduced noise, albeit with less gain. It can be clearly seen in the temporal pulse right at the soliton fission that the ABs on the pump pulse at $\Omega = -400$ is comparatively more well-defined than that of both the untriggered SC and the CW-triggered SC at $\Omega = -179.7$ (inset of Fig. 7(b)).

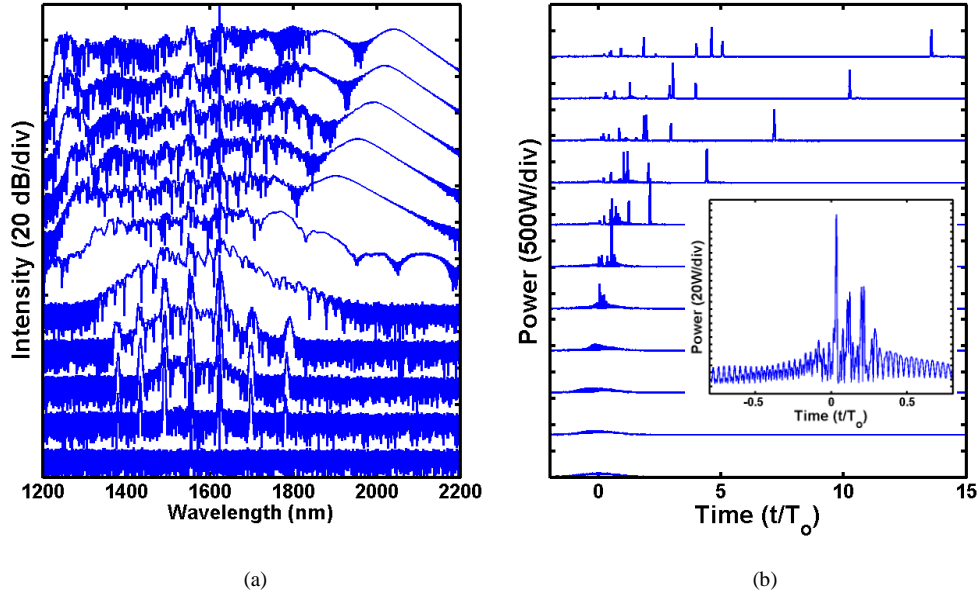(a)   (b)

Fig. 6. (a) Spectral and (b) temporal evolution of the CW-triggered SC generation ($\Omega = -179.7$, $\lambda = 1624$ nm). The spectra and temporal pulse shapes are shown in every 5 m (from bottom to top, $z = 0, 5, 10, \ldots,$ and 50 m). The inset shows the enlarged view of the temporal pulse at 20 m.
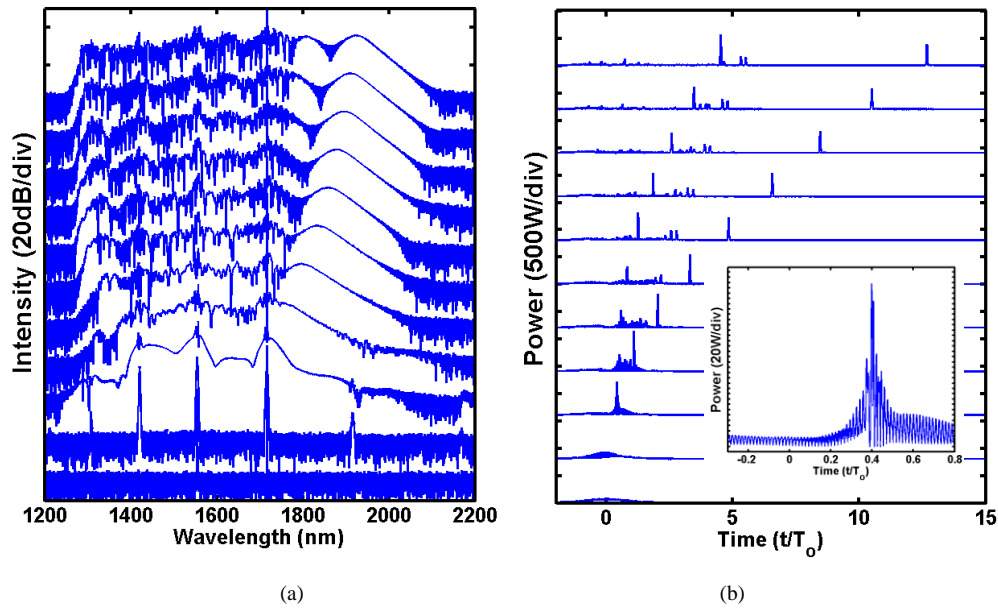
Fig. 7. (a) Spectral and (b) temporal evolution of the CW-triggered SC generation ($\Omega = -400$, $\lambda = 1716$ nm). The spectra and temporal pulse shapes are shown in every 5 m (from bottom to top, $z = 0$, 5, 10, …, and 50 m). The inset shows the enlarged view of the temporal pulse at 10 m.

Figures 5, 6 and 7 show that by tuning the wavelength of the CW-trigger, we can modify the initial condition of SC onset, more specifically the AB dynamics, to be either relatively more stochastic or more deterministic. This argument can be verified by studying the timing jitter of the Raman rogue soliton emerged from the initial soliton fission (Fig. 9). Figure 9 illustrates the temporal pulses corresponding the red-shifted components of SC (>1850 nm) in three different cases. This red-shifted part mostly captures the Raman soliton in SC spectrum. We can see that the pulses are randomly scattered throughout the 40-ps window for the case of untriggered SC (Fig. 9(a)). For the CW-triggered SC at $\Omega = -179.7$, the pulses are still widely scattered within ~15 ps (Fig. 9(b)). In contrast, the Raman soliton pulse ensemble is well defined and its timing jitter is as low as ~100 fs. This explains the high temporal coherence in the red-shifted Raman soliton whereas it has low coherence for the cases of untriggered SC and the CW-triggered SC at other Ω values, as shown in Fig. 3(b).
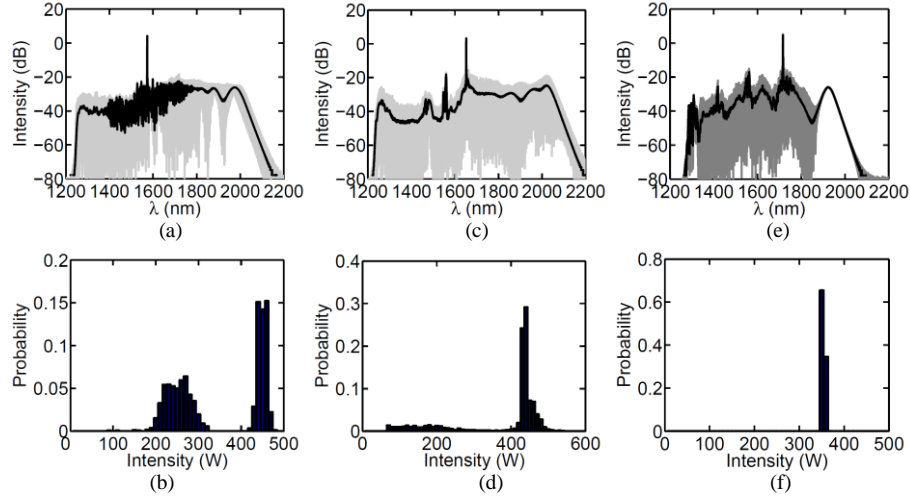
Fig. 8. CW-triggered SC spectra at (a) $\Omega = -50$, $\lambda = 1573$ nm (c) $\Omega = -250$, $\lambda = 1652$ nm (e) $\Omega = -400$, $\lambda = 1716$ nm. The individual spectra from the simulation ensemble (gray; for clarity only 50 shots are plotted) with the calculated average spectrum from the 1000 simulation runs (black curve). Histograms of the peak power distribution for the cases of (b) $\Omega = -50$, $\lambda = 1573$ nm, (d) $\Omega = -250$, $\lambda = 1652$ nm, and (f) $\Omega = -400$, $\lambda = 1716$ nm. The histograms are plotted for the 1000 events after a long-pass filter (>1850 nm) using 10 W bins.
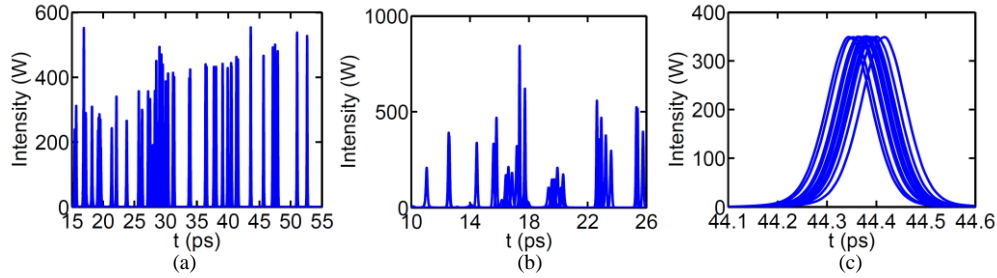

Fig. 9. Temporal pulses (for clarity, only 20 shots are plotted) after passing SC spectra through a long-pass filter (>1850 nm) for the (a) untriggered SC, (b) CW-triggered SC for $\Omega = -179.7$ and $\lambda = 1624$ nm, and (c) CW-triggered SC for $\Omega = -400$ and $\lambda = 1716$ nm.

Figure 8 further considers the pulse-to-pulse spectral and intensity variations at different CW-trigger wavelengths ((a), (b): $\Omega = -50$; (c), (d): $\Omega = -250$; and (e), (f): $\Omega = -400$). The shot-to-shot spectral variation is generally reduced, especially in the red-shifted Raman soliton in SC (Fig. 9(a), 9(c) and 9(e)), when compared with the untriggered SC (Fig. 2(a)). In particular, we again investigate the temporal fluctuation of the red-shifted components in SC (> 1850 nm). In general, as shown in Figs. 8(b), 8(d) and 8(f), adding the CW-triggers completely changes the intensity statistics when compared with the untriggered SC (Fig. 2(c)). Notably, Figs. 8(e) and 8(f) shows that for the case of $\Omega = -400$, the pulse-to-pulse stability can be maintained at a very high level. The statistical distribution of the pulse intensity has a standard deviation (calculated from 1000 events) as small as $0.01P_0$. Table 1 gives the overall summary of how the CW-triggers (at different wavelengths) affect the properties of SC in terms of the bandwidth, temporal coherence (both the overall coherence and the coherence of the red-shifted part of SC), and the pulse-to-pulse intensity stability (in terms of the standard deviation). Generally, the present study shows that adding the weak CW-trigger can enhance SC bandwidth and achieve moderate improvement in the overall temporal coherence and the pulse-to-pulse stability. In particular, the dependence of the bandwidth, temporal coherence, and pulse-to-pulse stability on the CW-trigger wavelengths are rather subtle. The variation of

the bandwidth as a function of the CW-trigger wavelength follows the opposite trend to that of the temporal coherence (as shown in Figs. 4(a) and 4(b) and Table 1). This feature might provide a new insight to understand how these SC characteristics (bandwidth and/or coherence), or in particular the Raman rogue soliton (or generally optical rogue waves), can be further manipulated by the CW triggering scheme.

Table 1. Comparison of the Effects on SC Characteristics by Different CW-Trigger Wavelengths (Untriggered SC is also Included)

	Untriggered SC	*Ω = –50*	*Ω = –179.7*	*Ω = –250*	*Ω = –400*
SC Bandwidth (at the −50dB level)	787 nm	815 nm	933 nm	873 nm	718 nm
Standard deviation (>1850 nm)	$2.7P_0$	$1.71P_0$	$2.1P_0$	$1.95P_0$	$0.01P_0$
Coherence (>1850 nm)	0.0038	0.0075	0.0059	0.006	0.745
Overall coherence	0.155	0.59	0.37	0.38	0.65

4. Conclusion

In conclusion, we performed a detailed numerical study on how the picosecond SC's properties can be influenced by a simple CW triggering scheme. In general, we showed that injecting the weak CW-trigger can enhance SC bandwidth and attain a moderate improvement in the overall temporal coherence and the pulse-to-pulse stability. It can be understood by that the higher-order coherent FWM components generated by the CW-trigger can create a more deterministic beating effect on the pump pulse. This essentially establishes a more well-defined AB condition in the presence of noise – a precursor of the soliton fission and other high-order effects which results in the onset of SC. While the CW-trigger accelerates the onset of SC and thus enhances the bandwidth, further improvement in bandwidth by the trigger does not necessarily lead to higher temporal coherence. Indeed, we observed that the bandwidth variation as a function of the CW-trigger wavelength exhibits the opposite trend to the temporal coherence variation. We found that it could be related to the interplay between the pump depletion (which leads to the dynamic MI spectral gain changes) and the coherent parametric conversion of the CW-trigger – leading to either a more deterministic or a more random initial AB evolution, depending on the trigger wavelength. This interplay could explain the striking feature that the Raman rogue soliton emerged in SC generation exhibits a high degree of temporal coherence and pulse-to-pulse intensity fluctuation at the longer CW-trigger wavelength.

In conclusion, we note that SC characteristics depend on a myriad of different parameters and initial conditions. For instance, different input noise conditions, higher-order dispersion parameters, and pump pulse widths (especially for longer pulses or even CW pumping) could result in different statistical properties of the original untriggered SC. This implies that the impacts of the triggering on SC properties would vary from case to case. Establishing a complete and unified understanding on the triggered-SC properties requires more extensive investigation which takes all the aforementioned parameters into consideration and studies how the interplay among them results in different triggering scenarios. Nevertheless, we anticipate that the results presented here would provide a valuable insight on how the initial soliton fission can be initiated in a more controllable manner such that a SC generation with high temporal coherence can be realized. This could pave the way to offer a further flexibility to actively engineer the temporal properties of SC, particularly for applications where real-time, ultrafast, and single-shot spectral measurements are critical.

Acknowledgments

Y. Cheung and Yi Qiu in the University of Hong Kong for providing the experimental parameters and the fruitful discussions.